JGR Space Physics

TECHNICAL REPORTS: METHODS

10.1029/2021JA029149

Calibrating Electrostatic Deflection of Charged Particle Sensors Using Ambient Plasma Measurements

Alexander C. Barrie[1,2], Conrad Schiff[2], Daniel J. Gershman[2], Barbara L. Giles[2], and David Rand[2,3]

[1]Aurora Engineering, Orono, ME, USA, [2]NASA Goddard Space Flight Center, Greenbelt, MD, USA, [3]A. I. Solutions, Greenbelt, MD, USA

Key Points:

- Cross correlation of multiple spin offset measurements can be used to measure pointing error of electrostatic steering instruments
- Statistical samples of cross correlation lead to accuracy of pointing knowledge an order of magnitude better than native angular resolution
- Pointing error for electrostatic steering can be calibrated in flight commanding, or post-corrected on the ground

Correspondence to:

A. C. Barrie,
alexander.c.barrie@nasa.gov

Citation:

Barrie, A. C., Schiff, C., Gershman, D. J., Giles, B. L., & Rand, D. (2021). Calibrating electrostatic deflection of charged particle sensors using ambient plasma measurements. *Journal of Geophysical Research: Space Physics*, *126*, e2021JA029149. https://doi.org/10.1029/2021JA029149

Received 22 JAN 2021
Accepted 15 JUN 2021

Abstract As space-based charged particle measurement pushes the technical envelope, resolution, both spatially and temporally, is ever improving. As such, the knowledge of the associated error must also improve. We present a method for correlating data collected from multiple sensors at different times in order to estimate the pointing error of each sensor. The method is demonstrated using flight data from the Dual Ion Spectrometer suite, part of the Fast Plasma Investigation on the NASA's Magnetospheric Multiscale mission. By looking at signals with sharp features in the direction of spacecraft spin, the relative error in look direction between sensors can be estimated with sub-degree precision, roughly 20 times better than the native resolution in the azimuthal (spin) direction. These sharp features appear in nature often enough that a sufficiently large sample size can be identified, using an automated filter of routine science data, to calibrate the system, or post correct measured data. The relative pointing error can then be trended over time to monitor the evolution/aging of the measurement system. These data inform calibration/correction methods, should the error grow to a point where science quality is adversely affected.

1. Introduction

Spacecraft instrumentation are often reliant on high voltage electronics, which must maintain accuracy over a multi-year mission life. Particle spectrometers are no exception and typically use high voltage electrostatic elements to filter incoming particles based on energy, or look direction (Carlson et al., 1982). It can be difficult to maintain knowledge of the accuracy of the electronics controlling these electrostatic components over the life of the mission, as components' performance changes due to radiation exposure, thermal cycling, and other aging phenomena. This is especially important when data from multiple sensors are combined to form a single image, as artificial discontinuities can be introduced at the sensor boundaries.

The Fast Plasma Investigation (FPI), a suite of plasma spectrometers on NASA's Magnetospheric Multiscale mission (MMS), utilize four dual top hat analyzers, each with four electrostatic look directions, on each of four identical satellites (Burch, Moore, et al., 2016; Pollock et al., 2016). An FPI science skymap captures a full sky image (32 azimuth, 16 elevation bins) over 32 logarithmically energy bins (2 eV–30 keV for ions, 6 eV–30 keV for electrons). The fastest resolution burst data captures a complete skymap every 150 ms for ions and every 30 ms for electrons. The 32 azimuthal bins (each 11.25° wide) are measured by four Dual Electron/Ion Spectrometers (DES/DIS). Each dual spectrometer has two sensor heads, which each sweep through four electrostatic deflection steering states. Each sensor head contains 16 discrete anodes, which simultaneously measure the 16 elevation bins to cover 180° of elevation (11.25° per bin.) The angular bins and associated look directions are shown in the top panel (a) of Figure 1. The power supply for FPI controls three stepping supplies (two deflection and one energy), each with a low (≈0–50 V) and high (≈50–5000 V) range. The applied voltage is leveraged by an analyzer and deflection constant to allow for energy and angle filtering up to the operational limit of 30,000 eV particles. Because the two heads share a power supply, a single applied voltage is set for both heads simultaneously. The decision was made early in the design of FPI to cross-wire the deflectors, meaning that the upper deflector of one head is wired to the lower deflector of the paired head (See (Pollock et al., 2016) for details of cross wiring implementation.) This allows for plasma moments to be calculated in 1/4 of the required time (7.5 ms for electrons, 20 ms for ions) using one deflection state's worth of data (Phan et al., 2018; Rager et al., 2018). The down side of this decision, however, is that the steering voltages cannot be optimally set for both heads simultaneously leading to induced

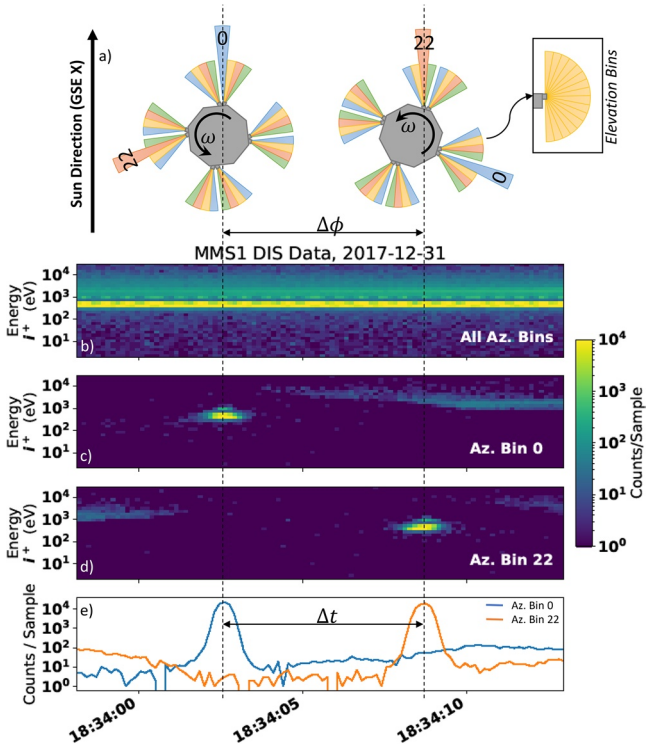

Figure 1. (a) Deflection states shown via colored fields of view. All states of a given color are measured simultaneously. Azimuthal bins 0 and 22, separated by 247.5° are highlighted to illustrate measuring the same signal at different times due to spacecraft spin. (b) energy-time (ET) spectrogram showing counts as a function of time and energy for the entire Dual Ion Spectrometer suite on MMS1, for a typical solar wind interval from December 2017. Note that counts are per energy/angle sample, as opposed to summed. (c and d) ET spectrograms of the same interval, including only the signal as measured by azimuthal bins 0 and 22 respectively, illustrating the signal shifting in time. (d) Count rates for azimuthal bins 0 and 22 over time, highlighting the peak in count rates correlated to pointing in the direction of the solar wind. Upper right box shows the elevation bins associated with each measurement.

errors in the look direction of the instrument, approximately one degree pre-launch for FPI.

Due to the large number of independent analyzers combining data to form a complete measurement of the observable phase space, discrepancies in calibration of the look direction are critically important as these can lead to artifacts in derived data products. These discontinuities over analyzer boundaries can also be useful; by measuring the same plasma over the course of a ≈20 s spacecraft spin, it is possible to uncover discrepancies in measurements between the analyzers with sufficient resolution and accuracy to perform a calibration of the high voltage stepping electronics, or post-correct data on the ground.

Many previous missions of similar sensors have relied on spacecraft spin to measure a full sky in azimuth, where multiple samples are taken over the course of a spin using the same sensor (Angelopoulos, 2009; Carlson et al., 2001; Escoubet et al., 2001). In these situations, there will be no relative error between measurements because they are all taken by the same sensor. Some instrument suites have utilized multiple sensors, notably JADE (three sensors) (McComas et al., 2017) and HYDRA (two sensors) (Scudder et al., 1995), in addition to FPI (eight sensors). As combining data from multiple sensors becomes more common, and increasingly complex, an understanding of the relative pointing error between measurements is critical.

By correlating multiple analyzers together, adjusting for spin phase, and fitting the resulting correlation vs angular offset, over many thousands of measurements, a consistent value of pointing error between two sensors, as a function of energy, emerges. This functional representation of pointing error with energy can then be converted into a functional relation for voltage error on the applied steering electrode. This process is illustrated in Figure 1, which shows a typical solar wind interval for DIS. While any plasma with large spatial gradients may serve for this purpose, solar wind is an excellent regime to perform this analysis as the plasma outflow from the sun provides ions collimated into a supersonic anti-sunward beam. The top panel (a) shows a spacecraft, spinning with rotational velocity, ω, measuring a nonisotropic plasma. Panel (b) shows the corresponding energy-time (ET) spectrogram for the interval. Panels (c and d) show the ET spectrogram for two of the 32 possible look directions (0 and 22, an offset in spin phase of 247.5°.) The bottom panel (e) shows the count rate of azimuthal bins 0 and 22. Together, the panels show that as the spacecraft rotates, a signal is measured in each azimuthal bin separated by a given spin phase and time. Note that although the nominal bin separation in azimuth is 11.25°, the azimuthal field of view (FOV) for a given bin is typically 4–6° for DIS, and 5–11° for DES, meaning that there are gaps in the instantaneous coverage. The range in FOV is due to the electrostatic steering, which performs slightly differently for different electrostatic look directions. By contrast, the elevation bins (upper right outlined box) are governed by a segmented anode leading to an elevation FOV equal to the bin spacing of 11.25° (Pollock et al., 2016).

As shown in Figure 1, the signal for azimuth bin 22 will be offset to the signal of azimuth bin 0 in time, δt, according to the separation of the two look angles, Δϕ, the spin rate, ω, and an error term, ϕerr (Equation 1)

$$\Delta t = \frac{\Delta\phi + \phi_{err}}{\omega} \quad (1)$$

The error term, ϕerr represents the error in the expected look direction, not accounted for by the geometric separation, of the two azimuthal locations and can be uncovered by calculating the time separation of the two distributions, Δt. The error is a convolution of multiple error sources that fall into one of two categories:

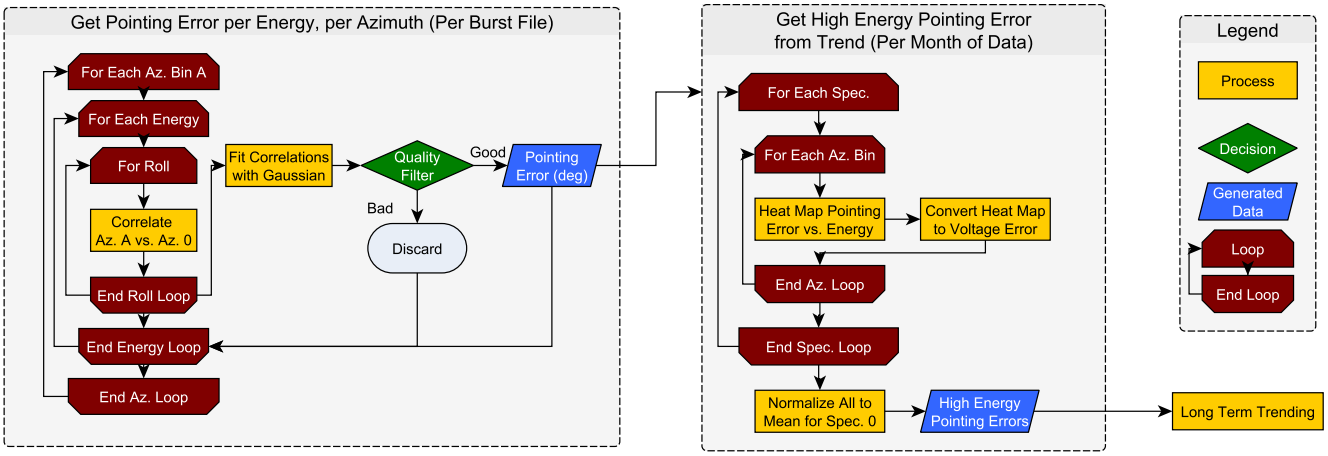

Figure 2. Flowchart of the algorithm. The left box is performed on each data file and generates, the pointing error for each azimuthal bin at each energy, and subsequently filters the results, allowing only plasma with sufficiently sharp, time stationary features. The right box shows how these data are analyzed statistically.

1. Random Error due, primarily, to fluctuations in the measured environment over time.
2. Systematic Pointing Error that is consistent over all measurements due to the on-board configuration of the sensors themselves.

By inspecting many intervals over time, the random error will naturally cancel out allowing the systematic pointing error to reach a statistically significant level such that it can be measured. This allows for two potential processes:

1. Correcting the pointing direction of plasma measurements on the ground by updating the unit vectors used in the phase space distributions and ensuing moment integrals.
2. Calibrating the voltages for electrostatic deflection used to measure given look directions for future measurements.

Note that this algorithm depends only on finding a feature in the surrounding plasma that lasts in time longer than the calibration duration (a single 20s spin) and not on how that feature is oriented with respect to Earth's magnetosphere. The filter mechanisms that are in place (Figure 2) ensure that such time-stationary features can be identified. The solar wind is used only as a convenient example of an environmental structure differentiated in direction that remains essentially time stationary. As shown in Section 3, once we applied this method to FPI in-flight data, we found the identified errors are not sufficiently large enough as to warrant generating and uploading a new voltage table to the spacecraft, however corrected look direction vectors can be applied for regions of scientific interest that warrant added precision.

2. Algorithm and Example Results

Figure 2 shows the process for filtering science data to find suitable signals, and subsequently cross correlating them. Burst resolution data for MMS/FPI are typically divided into files on the order of a few 10s of seconds. Given that an MMS spin is ~20 s, each burst resolution data file is on the order of a 1–5 spins. Each of the eight analyzers on a given spacecraft observes the same plasma environment, in a spinning reference frame, several times, assuming time stationarity of the plasma over the course of the measurement (intervals selected via filtering.) As such, the data from one analyzer can be compared to that of another using a correlation technique. To do this, each data array is split into energy shells, then each shell is “rolled” in time (a standard circular shift of the array, such that [1,2,3] becomes [2,3,1]) by varying amounts and each iteration of the roll is correlated with the data from azimuth (look direction) 0. Due to spacecraft spin, and the measurement cadence of the DIS (150 ms), each point in the correlation corresponds to ≈ 2.7° of rotation in spin phase (for electrons, which measure faster, this would be closer to 0.5°.) While the DES time cadence is advantageous, DIS was chosen as the focus of this study because ions tend to be more directional than electrons, making this analysis more applicable for ions. The roll is performed to the expected location

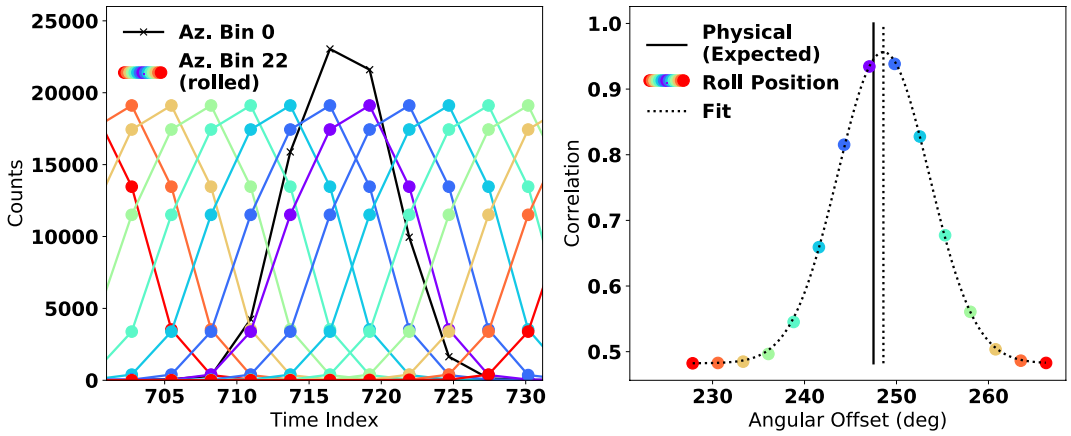

Figure 3. Solar wind data observed in azimuth bin 22 rolled in time and correlated against azimuth bin 0, individual shifted (rolled) distributions (a, left) and a fit to the resulting correlations between each rolled data set and azimuth bin 0 (b, right). Bin 0 reports a higher absolute magnitude of counts than Bin 22 due to a slightly higher detection efficiency.

(offset based on physical separation of analyzers and measured spin rate, accounted for in Equation 1 by $\Delta\phi/\omega$), and up to +/− 20° in spin phase (typically +/− 7 points in time.) A correlation of the rolled measurement (counts vs. time) for the chosen azimuthal bin and azimuthal bin 0 is performed via the numpy corrcoef function (Harris et al., 2020). This function returns a correlation for every point in the data set (each position in time). The mean of all correlation values forms the "true correlation" between the two sets of data.

Figure 3 (left) shows this correlation of azimuth bin 22 against azimuth bin 0 for one of the DIS for a sample burst data file. The black curve shows a signal from solar wind ions passing over azimuth bin 0 as the spacecraft rotates. The colored curves show the same signal passing over azimuth bin 22, with the distribution being rolled in time to different points ranging from the approximate expected location (purple) to ≈ +/− 20° off of expected (red). The resulting correlation as a function of roll is shown in Figure 3 (right). Each colored point shows the correlation for a given amount of roll (the colored curves from left panel.) Because the amplitude varies from ≈0.5 to 1, these are then fit to a modified Gaussian distribution, the peak of which is assumed to be the true offset between the two azimuthal look directions in spin phase, as in Equation 2.

$$y = a\exp\left(-\frac{(x-x_0)^2}{2\sigma^2}\right) + a_b \tag{2}$$

The amplitude, a, peak location, x0, width (standard deviation), σ, and the ambient isotropic background level, ab, are all fitted parameters. The ambient isotropic background refers to the level at which the the plasma becomes similar enough in angular space that the relative rotation (roll) of the data no longer reduces the measured correlation (i.e., the floor shown in the right panel of Figure 3 at around 0.48.) Because the azimuthal resolution is 11.25°, the expected separation between the look directions for azimuths 0 and 22 would be (22-0)*11.25 = 247.5°. In this example, the peak of the fit shows an offset closer to 248.5, or an error of about a degree in look direction.

This correlation is performed for all azimuthal bins, relative to bin 0, and a suite average of the error is taken, which is then assigned to be the error associated with bin 0 itself and subtracted from all other bins. Plasma regions that were not stationary in time, were too isotropic to differentiate look direction, or were otherwise ill suited to this effort, were discarded by a two step filtering process (left box, Figure 2): 1. a threshold was applied on the covariance (max of 1%) returned by the fitting algorithm, and 2. the standard deviation of the Gaussian must be less then 10°. The covariance of the Gaussian primarily

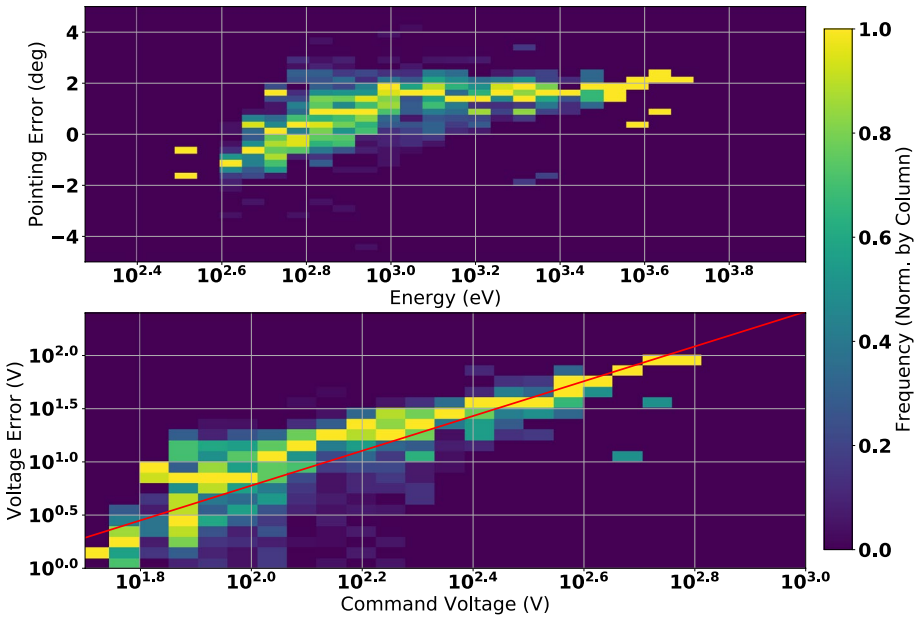

Figure 4. A statistical histogram of pointing error versus energy for a single spectrometer, accumulated over a span of about three months of operation. Data is for DIS1 on MMS1. The top panel shows pointing error directly as a function of energy target. The bottom panel shows the voltage error associated with the derived pointing error (i.e., after applying Equation 3.) Both panels are normalized by sample size per (energy, top/command voltage, bottom) bin for clarity. A linear fit (red) was created from the raw scatter data, prior to binning and normalization.

serves as the filter for stationarity in time. A perfectly stationary plasma will generally result in a fit shape that is a near perfect Gaussian (hence why a Gaussian was chosen), however a shifting plasma over the course of a spin will result in asymmetry around the peak, which can then be identified in the covariance of the fit. The width of the Gaussian (max of 10°) is primarily used to filter out plasma that is near isotropic. A sensor in these regions may see similar plasma in many locations leading to wide Gaussian with an uncertain peak location and an erroneous offset error estimation. Typically, the best location for this correlation is in the solar wind due to its stability and collimation (virtually all solar wind data passed the filter), however suitable data was found in all measured regions of the magnetosphere (roughly 10% of data taken around the magnetopause, MMS's primary day-side measurement region).

The offset in look direction can then be inspected as a function of energy. This is shown, statistically over about 2,000 intervals, in Figure 4 (top panel) for one of the DIS units on MMS1. A clear curve is evidenced in the estimate of pointing error as a function of energy, indicating reproducible results over many measurements. The pointing error at the low end of the energy range is negative. The pointing error then increases, through 0, up to a positive error, where it is roughly constant over the remainder of the interval. The knee in this curve, resulting in a downturn in the look angle error, is due to the convolution of the deflection with the energy discrimination. Deflection voltage, VDEF for a given deflection angle, ϕ, is related to energy, E as:

$$V_{DEF} = \frac{\phi E}{C_A C_D} \tag{3}$$

where CA and CD are constants governing the energy analyzer (≈5.1), and the deflection electrodes (≈20.8) (Carlson et al., 1982, 2001; Pollock et al., 2016). Converting to voltage error per volt, the lower panel of Figure 4 shows an approximately linear relationship for voltage error within the power supply. A linear fit to the raw scattered data is shown in red.

The uncertainty of the calculation can be estimated when each vertical slice (energy bin) is histogrammed over the pointing error and the resulting histogram is fit to a Gaussian distribution (Equation 2). The peak of the fit is asserted to be the pointing error, and the width of the Gaussian is the estimation of uncertainty. While this approach for estimating uncertainty may not be perfect, it was found by random sample to be more representative than a standard deviation. The peak of this fit also better approximates the most likely true pointing error than any of the mean/median/mode. This particular fit has an average uncertainty of around 20%. A more quantitative illustration of uncertainty is covered in Section 3. This uncertainty, corresponding to the random error mentioned above, is primarily due to (in assumed order of importance):

1. Low counting statistics affect the results at the low and high ends of the measurement space (i.e., there were not as many suitable plasma intervals at the lower and higher energy shells.)
2. The plasma is assumed to be stationary over the course of at least a full spacecraft spin (20s) which is not strictly true.
3. While the data are filtered based on the perceived quality of the correlation, the correlations are still not perfect, nor are the Gaussian fits, leading to some random statistical error.
4. There is quantization in the command words that assign voltages. This is a larger effect at lower commanded voltages of both energy and deflection. (Pollock et al., 2016)

Even if the uncertainty could be eliminated and a perfect correlation could be achieved, there would still be some deviation from linearity, particularly at the low end. This is also due to several factors, in order of assumed importance:

1. A kink in the curve is often present, due to:
   (a) The deflection voltage is proportional to the energy, which is controlled by a separate stepper supply (Pollock et al., 2016). This means that the deflection error is compounded by errors in the energy analyzer voltage. Note that Equation 3 is a relation between deflection voltage and energy; the energy filtering voltage is also subject to error.
   (b) Errors in the form of a static offset in voltage have a greater effect for lower applied voltages (i.e., a constant error of 1 V will more strongly influence an applied voltage of 10 V than 100 V.)
   (c) A knee in the curve can then be introduced when the energy stepper changes operating mode (low to high voltage range or vice versa) at a different time than the deflection stepper. The deflection voltage is typically around 70% of the energy discrimination voltage for the larger deflection, and around 30% for the lesser deflection state. The high and low voltage ranges are defined the same for all supplies, however, leading to range changes at different times for deflection and energy discrimination.
2. The errors shown here are not absolute errors of the power supply, but rather are errors relative to the existing calibration, which was performed pre-launch (Pollock et al., 2016). While every command voltage was verified, it was not possible to verify performance at every energy/deflection combination under vacuum, measuring particles. Rather, a spot check at several energies and look directions was performed under beam test. See (Pollock et al., 2016) for full description of FPI ground calibration. This is not known to be a major source of error for the current FPI calibration, but is noted here to emphasize that if a nonideal calibration were to be uploaded to the spacecraft, this would result in potential nonlinearity in the intensity plot shown in Figure 4.
3. As shown in (Barrie et al., 2019; Toledo-Redondo et al., 2019), incoming particle trajectories can be altered in an asymmetric way by the spacecraft plasma sheath. The result of this effect, in this context, is a systematic shift in the perceived separation of two azimuthal bins. This effect is most prominent below ≈50 eV, however, the effect can be seen up to ≈1,000 eV in elevation/azimuth combinations lining directly up with the MMS wire booms. There are only four such look directions out of 512 that are in line with the wire booms, however, so the affect is assumed to be a minor contributor here.
4. Finally, the spectrometers have slightly different performance characteristics due to part and assembly variations.

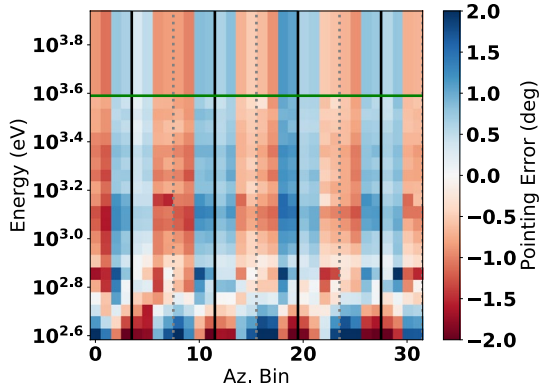

Figure 5. Average pointing error on MMS1 DIS units over energy and azimuthal look direction. The green line represents energies above which an extrapolated value was used. Solid black line separates dual spectrometers, dashed gray line separates heads of a dual spectrometer. Note that az. bin 0 separates the two heads of a dual unit.

3. Results for MMS/FPI-DIS

Figure 5 shows the average pointing error for all of the DIS on the MMS1 spacecraft as a function of energy and azimuthal bin using the same data intervals as Figure 4. For a given azimuthal look direction bin (vertical stripe) a transition can be seen where the look direction crosses from ≈positive 1° to negative 2° or vice versa. This is consistent with the example shown in Figure 4.

A clear red/blue striping is evident implying a systematic, alternating pointing error. This is due to the fact that the dual sensors share a common power supply and are crosswired. As noted in the figure, four successive azimuth bins belong to the same sensor head (four deflection states), and eight successive bins belong to a paired DIS, sharing a common power supply. This means that the upper deflector of one sensor and the lower deflector of the paired sensor share a common voltage (Pollock et al., 2016). Because the upper and lower deflectors have slightly different electrostatic steering properties, a single command voltage cannot be set that ideally commands both heads to the correct look direction steering voltage; a midpoint for look direction was therefore used. The observation of this design effect in the derived results provides a strong, independent validation of our approach. Because there were not a sufficient number of intervals that passed the filter at the highest energy bins, we extrapolated from the mid range energies using the mean of the highest 10 energies that were individually calculated. The minimum energy bin represents the lowest measured energy in the high voltage operating mode of the deflection stepper.

Figure 5 represents the state of the electrostatic steering with no indication of potential changes over time. To track how this process evolves in time, the high energy pointing error (value assigned above the green line, ≈1° in Figure 5) can be used as a proxy for monitoring changes and trended for each azimuthal bin (look direction). A long term monthly trend for a sample DIS sensor is shown in Figure 6, with each of the four lines corresponding to one of the four deflection states of the sensor. While some minor drift is evident, the pointing error is quite stable over a period of over four years, with the drift lying within the band of uncertainty. Each point represents a month of data collected, with the number of samples included used as a sample weight for the linear fit routine. For each month of data, a histogram was taken with a Gaussian

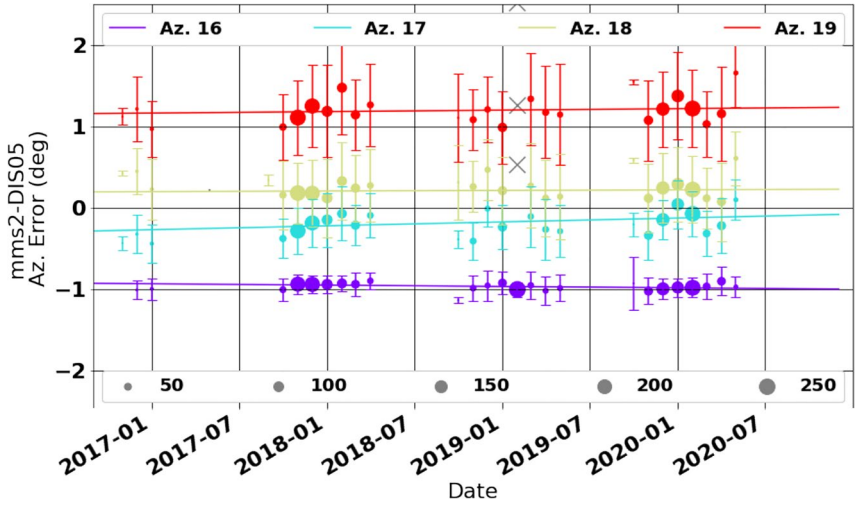

Figure 6. Time trend of high energy pointing error for the four deflection states of a sample Dual Ion Spectrometer sensor head. Each of the four deflection states (Az. Bin) have a linear trend line, weighted by the number of samples. Some outliers are excluded (gray x), via the scikit_learn ransac algorithm (Pedregosa et al., 2011). Gaps in time are due to seasonal use of voltage stepper tables.

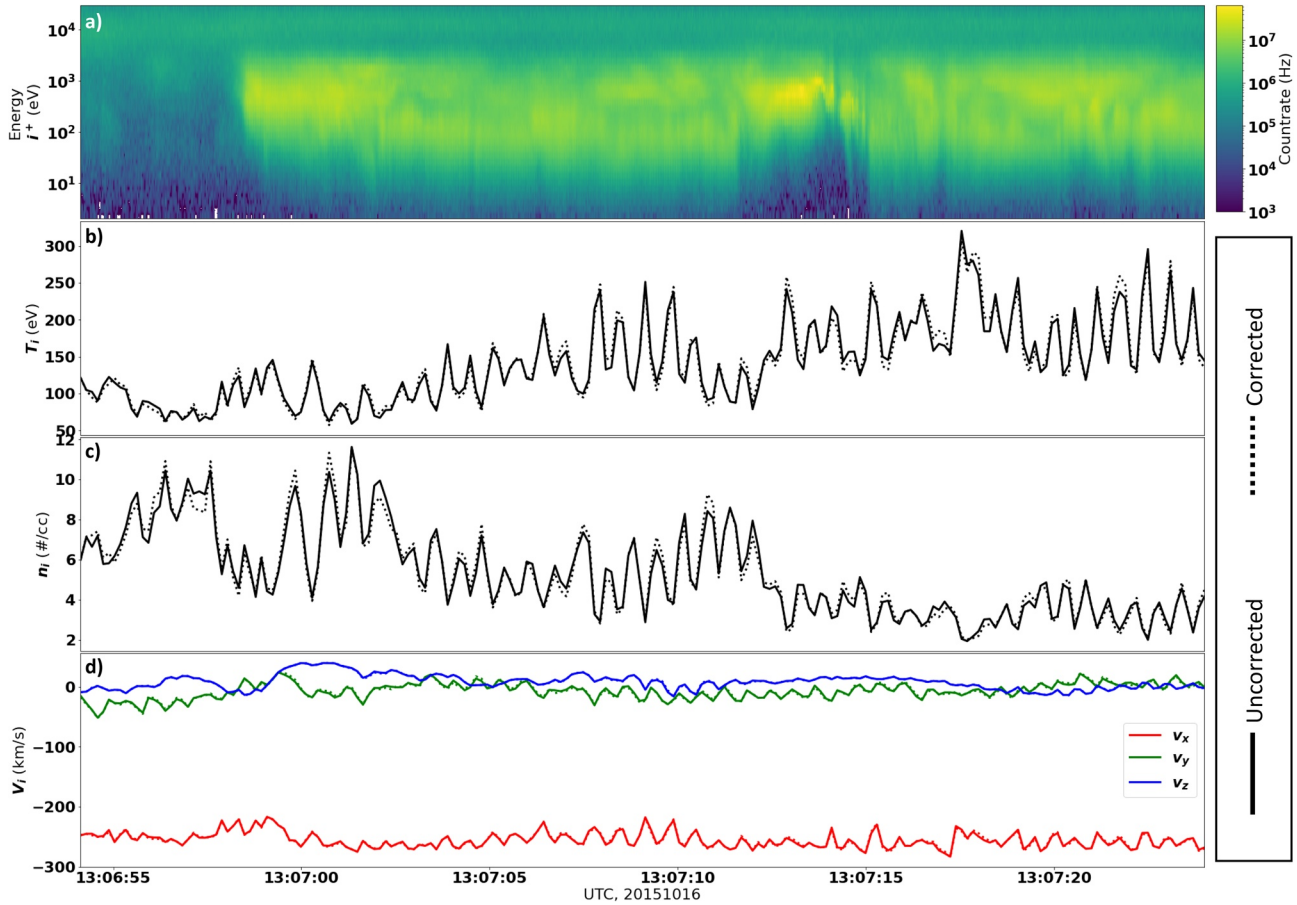

Figure 7. Top panel (a) shows a standard ion energy time spectrogram of the identified diffusion region from Ref (Burch, Torbert, et al., 2016). Remaining panels show the (b) ion temperature, T, (c) number density, n, and (d) velocity $\vec{v}$. For each of the line graphs (b, c, and d), the solid line represents the integrations carried out with the standard look directions and the dashed line represents the integrations carried out with the look directions corrected as per Figure A1.

(Equation 2) fit performed on the resulting distribution. The peak of this Gaussian fit is assigned as the calculated offset for that month and the width of the Gaussian is assigned as the uncertainty (error bars in the figure.)

Similar plots for all DIS units are shown in the Appendix (Figure A1). While this particular analysis was performed using higher energy data (i.e., the high range of the power supply) for the purpose of counting statistics, the majority of the controlling circuitry is shared between the low and high range. In particular, the control DAC and the error amplifier, the circuit portions which have the greatest potential for nonlinearity, are shared for both ranges. As such, and confirmed by several spot checks, the FPI look direction offsets presented in the Appendix can be used for both the low and high energy ranges.

It is again clear that the absolute pointing error, regardless of trend, is nonzero owing to the cross-wiring of the power supply. The four plotted pointing errors (from the four deflection states) are generally centered around zero, however, indicating that the instrument is optimally balanced. Because this calibration is relative, comparing two look directions to each other, one might worry that if all azimuth bins drifted by the same pointing error, the correlation would not reveal the error. This is not a concern in practice, however, because of the cross-wiring: a given drift in HVPS performance would have an opposite effect on the two shared sensor heads rather than an equivalent effect. While the deviation over time is generally small (≈0.1°), there are a few trend lines that appear steeper and show close to a full degree of change over time. Some of this perceived drift is due to the trend line being weighted

by the number of samples as a way to minimize the effect of outliers, and some of it is due to the normalization to the mean (mean applied to bin 0 and subtracted from all others). Even if a drift of a full degree is taken as truth in some cases, the overall pointing error is still within the uncertainty of the calculation.

To assess the impact of this pointing error, standard plasma moments were calculated for the reconnection region identified in (Burch, Torbert, et al., 2016) with and without corrected look directions. Figure 7 shows that while some change in the plasma moments is evident, the change is small relative to the periodicity already present in the signal. This larger periodicity is influenced by gaps in measurement space, where some portion of the signal is not detected. This missing signal is a larger overall effect than any error introduced by the off pointing.

If the drift in pointing error becomes large, then this knowledge of pointing error may be used to calibrate the system. This calibration could take one of two forms:

1. The applied command voltage could be adjusted. The voltages would be altered based on the calculated voltage error as in Figure 4 (bottom panel). In the case of FPI, this would be accomplished by updating a set of voltage stepper tables stored in EEPROM(Pollock et al., 2016).
2. Updated look directions could be included in velocity moment integrals for specific science intervals of interest. This is the approach taken in the sample correction for Figure 7.

Updating the on board voltages, as described in Option 1, is operationally complex and would only be undertaken if a severe pointing error became evident (>1/2 bin, or 5.625°). Corrected look directions in plasma moment integrals, as outlined in Option 2 and used in Figure 7, however, may be applied to regions of particular scientific interest.

4. Conclusion

Many particle analyzers have angular bin size of several degrees. FPI, the system examined here, has a fairly typical bin size of 11.25°. This work shows a method by which the pointing error in the electrostatic deflection can be resolved with sub degree accuracy, or about a factor of 20 less than the native angular bin size.

The method proposed here uses correlations between multiple sensors, in the direction of spin phase, to estimate the relative difference between two electrostatic deflection look directions. This is not an absolute calibration, as each deflection angle error is measured to a suite average. An absolute calibration could potentially be obtained by using a known directional signal, such as the Sun. It should be noted, however, that a primary strength of this approach is that it does not require a specific environment, only that the plasma possess a significant directional drift, resulting in anisotropy of the velocity distribution function as a function of look direction in the reference frame of the spacecraft, and also that the plasma is ≈stable over the course of a complete spacecraft spin.

It should be noted that this method does require multiple sensors, and a single sensor that forms an image over the course of a spin would not need this type of analysis. As missions are increasingly looking at faster time resolutions, however, it is increasingly common for spacecraft to utilize multiple sensors in order to meet timing requirements. As such, an accurate method for determining pointing error will be a valuable addition to the in-situ measurement toolkit.

Appendix A: Long Term Trending for MMS/FPI

This work serves to outline a method by which pointing error may be evaluated from multi-sensor particle counting instruments. Because the MMS/FPI suite was used as the case study for this effort, a sample multiyear result of this process is shown in Figure A1 for the DIS sensors. Pointing error is calculated using of a month of measurements for each data point. All date for the included month are Due to seasonal operation schedules, there are some months that do not have data shown.

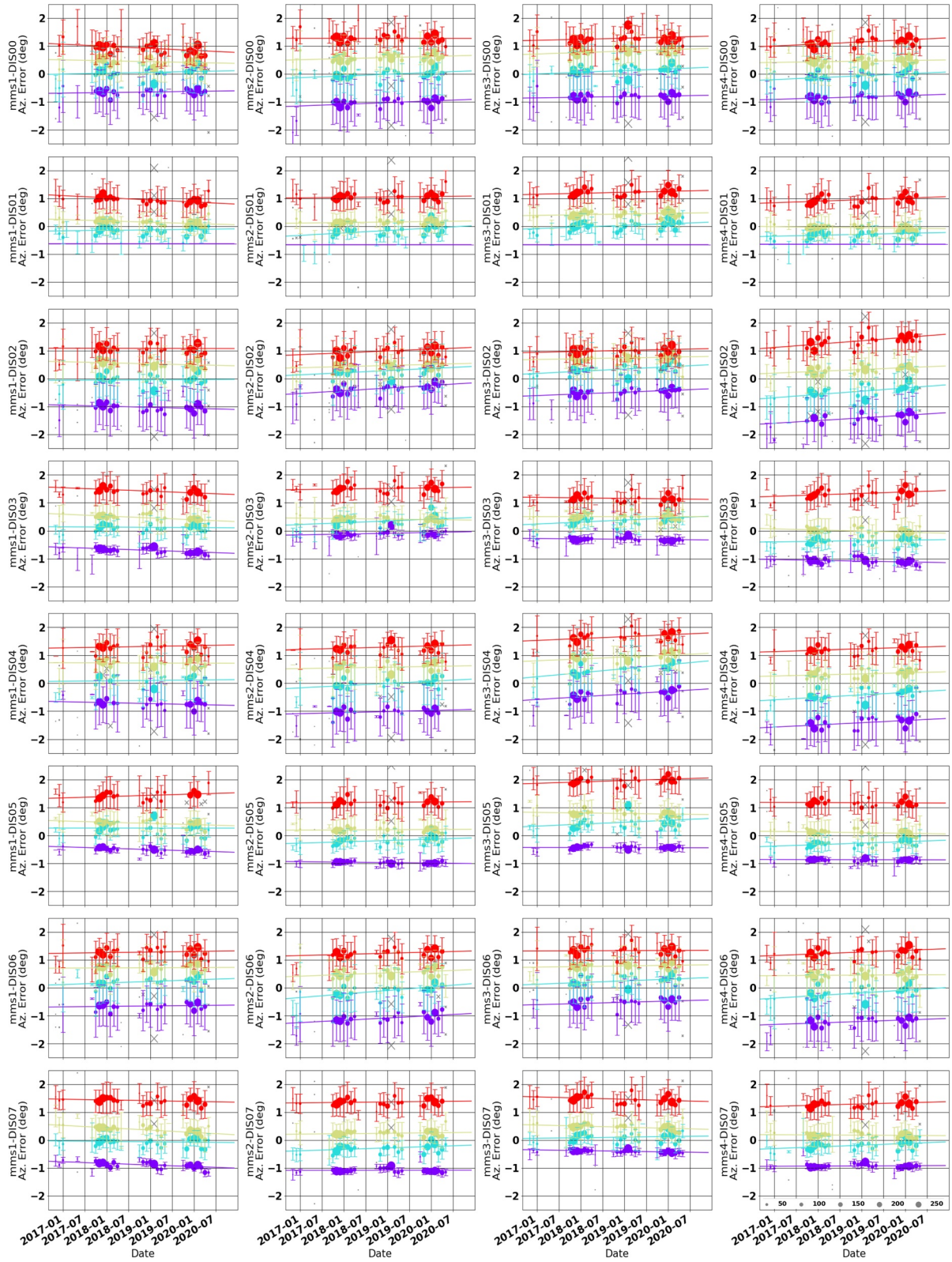

Figure A1. Pointing error curves for all Dual Ion Spectrometer units. The four colors represent the four look directions for a given sensor head, similar to Figure 6. Marker size indicates number of samples for a given month. A gray 'X' indicates a point that was disregarded as an outlier, while colored 'O' are included. Lines with no symbols (purple, second row from top) are the reference spectrometer (Az. bin 0) which are taken as the suite average offset. Error bars are calculated as described in Section 3.

Data Availability Statement

Source data is available from the MMS Science Data Center (https://lasp.colorado.edu/mms/sdc/public/).

Acknowledgments
Funded by NASA and the MMS mission.

References

Angelopoulos, V. (2009). *The THEMIS Mission* (pp. 5–34). Springer. https://doi.org/10.1007/978-0-387-89820-9_2

Barrie, A., Cipriani, F., Escoubet, C., Toledo-Redondo, S., Nakamura, R., Torkar, K., et al. (2019). Characterizing spacecraft potential effects on measured particle trajectories. *Physics of Plasmas*, *26*(10), 103504. https://doi.org/10.1063/1.5119344

Burch, J., Moore, T., Torbert, R., & Giles, B. (2016). Magnetospheric multiscale overview and science objectives. *Space Science Reviews*, *199*. https://doi.org/10.1007/s11214-015-0164-9

Burch, J, Torbert, R, Phan, T, Chen, L.-J, Moore, T, Ergun, R, et al. (2016). Electron-scale measurements of magnetic reconnection in space. *Science*, *352*(6290).

Carlson, C., Curtis, D., Paschmann, G., & Michel, W. (1982). An instrument for rapidly measuring plasma distribution functions with high resolution. *Advances in Space Research*, *2*(7), 67–70. https://doi.org/10.1016/0273-1177(82)90151-x

Carlson, C., McFadden, J., Turin, P., Curtis, D., & Magoncelli, A. (2001). The electron and ion plasma experiment for fast. In *The fast mission* (pp. 33–66). Springer. https://doi.org/10.1007/978-94-010-0332-2_2

Escoubet, C., Fehringer, M., & Goldstein, M. (2001). Introduction the cluster mission. *Annales Geophysicae*, *19*, 1197–1200. https://doi.org/10.5194/angeo-19-1197-2001

Harris, C. R., Millman, K. J., Walt, van der, S. J., Gommers, R., Virtanen, P., Cournapeau, D., et al. (2020). Array programming with NumPy. *Nature*, *585*(7825), 357–362. https://doi.org/10.1038/s41586-020-2649-2

McComas, D., Alexander, N., Allegrini, F., Bagenal, F., Beebe, C., Clark, G., et al. (2017). The Jovian auroral distributions experiment (jade) on the juno mission to jupiter. *Space Science Reviews*, *213*(1–4), 547–643. https://doi.org/10.1007/s11214-013-9990-9

Pedregosa, F., Varoquaux, G., Gramfort, A., Michel, V., Thirion, B., Grisel, O., & Duchesnay, E. (2011). Scikit-learn: Machine learning in Python. *Journal of Machine Learning Research*, *12*, 2825–2830.

Phan, T., Eastwood, J. P., Shay, M., Drake, J., Sonnerup, B. Ö., Fujimoto, M., et al. (2018). Electron magnetic reconnection without ion coupling in earth's turbulent magnetosheath. *Nature*, *557*(7704), 202–206. https://doi.org/10.1038/s41586-018-0091-5

Pollock, C., Moore, T., Jacques, A., Burch, J., Gliese, U., Saito, Y., et al. (2016). Fast plasma investigation for magnetospheric multiscale. *Space Science Reviews*, *199*, 331–406.

Rager, A., Dorelli, J., Gershman, D., Uritsky, V., Avanov, L., Torbert, R., et al. (2018). Electron crescent distributions as a manifestation of diamagnetic drift in an electron-scale current sheet: Magnetospheric multiscale observations using new 7.5 ms fast plasma investigation moments. *Geophysical Research Letters*, *45*(2), 578–584. https://doi.org/10.1002/2017gl076260

Scudder, J., Hunsacker, F., Miller, G., Lobell, J., Zawistowski, T., Ogilvie, K., et al. (1995). Hydra 3-dimensional electron and ion hot plasma instrument for the polar spacecraft of the ggs mission. *Space Science Reviews*, *71*(1–4), 459–495. https://doi.org/10.1007/bf00751338

Toledo-Redondo, S., Lavraud, B., Fuselier, S., André, M., Khotyaintsev, Y. V., Nakamura, R., et al. (2019). Electrostatic spacecraft potential structure and wake formation effects for characterization of cold ion beams in the earth's magnetosphere. *Journal of Geophysical Research: Space Physics*, *124*(12), 10048–10062. https://doi.org/10.1029/2019JA027145